International Journal of Environmental Science and Technology (2026) 23:381
https://doi.org/10.1007/s13762-026-07162-9

ORIGINAL PAPER

Enhanced sulfate radical generation through bimetallic Ni–Cu catalysts synthesized in a fluidized bed for rapid RB5 degradation

P. Družaitė[1] · D. Martuzevičius[1] · T.-H. Ha[2] · M.-C. Lu[2,3]

Received: 16 December 2025 / Revised: 6 March 2026 / Accepted: 2 April 2026

Abstract

The treatment of dye-containing wastewater remains a significant environmental challenge, as persistent azo dyes such as Reactive Black 5 (RB5) are resistant to conventional oxidation and biological processes. In this study, we propose a Fe-free advanced oxidation strategy based on sodium persulfate activation using Ni–Cu bimetallic catalysts synthesized via fluidized-bed homogeneous crystallization (FBHC), with a systematic comparison to catalysts prepared by conventional jar-test precipitation (JAR). The novelty of this work lies in coupling FBHC synthesis with persulfate activation to produce highly reactive, amorphous Ni–Cu catalysts capable of rapid pollutant degradation under near-neutral conditions, thereby overcoming the sludge generation and pH limitations associated with traditional Fenton systems. Using 100 mg L^{-1} RB5 as a model contaminant, the FBHC-derived catalyst achieved > 90% decolorization within 10 min and 70.7% TOC removal within 5 min, significantly outperforming the JAR-derived material. Kinetic analysis indicated that the degradation followed the Langmuir–Hinshelwood model, suggesting a surface-controlled reaction pathway. Radical scavenging and EPR analyses identified $SO_4\cdot^-$ and $^1O_2$ as the dominant reactive species, with minor contributions from ·OH and negligible involvement of $O_2\cdot^-$. Overall, this study demonstrates that (i) FBHC is an effective method for fabricating highly reactive bimetallic catalysts and (ii) the Ni–Cu/persulfate system represents a rapid, Fe-free oxidation process operable under mild pH conditions, offering a promising strategy for efficient and scalable textile wastewater treatment.

Keywords Fluidized-bed reactor · Reactive black 5 · Chemical precipitation · Advanced-oxidation process · Sulfate radical

Introduction

The rapid development of cities and industries over the past decades has led to significant environmental challenges that threaten essential natural resources, with water being one of the most critical (Santos et al. 2021). Among various toxic compounds, synthetic dyes are prominent pollutants commonly found in textile industry effluents (Silva et al. 2022; Han et al. 2024). Azo dyes, which account for the majority of globally produced synthetic organic dyes, are widely used in the textile sector due to their cost-effectiveness and favorable chemical properties. Reactive dyes are particularly notable for their high color stability, low biodegradability, and significant toxicity. Reactive Black 5 (RB5), a widely used and chemically stable azo dye, is highly resistant to conventional treatment processes and is frequently detected in wastewater streams (Zhou et al. 2019). Consequently, RB5 is often employed as a model compound for evaluating advanced oxidation and catalytic degradation methods.

Various physicochemical treatment techniques, including coagulation, flocculation, and adsorption, are limited by high operational costs and the generation of substantial amounts of sludge as byproducts (Signorelli et al. 2021; Gul et al. 2023). In contrast, advanced oxidation processes (AOPs) are widely recognized as one of the most effective approaches because they degrade pollutants rather than merely concentrating them (Li et al. 2023). Extensive research on dye-containing wastewater has led to the development of various

---

Editorial responsibility: S.Mirkia.

✉ M.-C. Lu
mmclu@nchu.edu.tw

[1] Faculty of Chemical Technology, Kaunas University of Technology, Kaunas, Lithuania

[2] Department of Environmental Engineering, National Chung Hsing University, Taichung, Taiwan

[3] Innovation and Development Center of Sustainable Agriculture, National Chung Hsing University, Taichung 402, Taiwan

AOPs, such as ozonation (Sari et al. 2023), Fenton (Lucas and Peres 2006), permanganate (Wang et al. 2024), and persulfate-based processes (Anthony and Doğan 2023). These methods generally rely on the rapid reaction of hydroxyl radicals (·OH) with organic contaminants, typically employing oxidants in combination with catalysts, light, or ultrasound to remove persistent organic pollutants. Compared with conventional oxidants, AOPs exhibit significantly higher oxidation potential, enabling ·OH to partially or completely degrade toxic substances and their byproducts, including dyes, chemicals, and pesticides (Zhu et al. 2023a). By generating reactive oxygen species (ROS), organic pollutants can be effectively mineralized into harmless end products such as CO_2 and H_2O. Key advantages of AOPs include rapid reaction kinetics, non-selective oxidation, and minimal secondary pollution (Li et al. 2023). However, conventional AOPs still face several intrinsic limitations that hinder their practical application, including sludge generation, strong pH dependence, and high operational costs (Malik and Patel 2023).

One approach that addresses these drawbacks is the heterogeneous Fenton-like reaction, which eliminates the need to maintain strongly acidic conditions (pH 2–4) and significantly reduces sludge formation while still enabling effective pollutant removal (Liu and Wang 2023). Hydrogen peroxide (H_2O_2) and persulfate (PS) are among the most commonly used oxidants in AOPs for generating reactive species (Fadaei et al. 2021). In particular, sulfate radicals ($SO_4 \cdot^-$) have attracted increasing attention as promising alternatives due to their higher oxidation potential ($E^0 = 2.5$–3.1 V), longer half-life (30–40 μs compared with ~ 10^{-3} μs for ·OH), and effectiveness over a wider pH range. These $SO_4 \cdot^-$ radicals are typically generated from persulfate (PS) or peroxymonosulfate (PMS) through various activation methods, including thermal, alkaline, ultraviolet irradiation, activated carbon, transition metals (such as Fe^{2+}, Cu^{2+}, Mn^{2+}, and Co^{2+}), ultrasound, and hydrogen peroxide (Malik and Patel 2023). Nevertheless, Fe-based activation is constrained by its narrow optimal pH range (≈2.8–3.5), the generation of iron sludge, and the risk of secondary contamination from dissolved iron species, which considerably limit its practical applicability. Consequently, increasing research efforts have been directed toward Fe-free activation approaches, which offer broader operational flexibility and improved environmental compatibility (Jiang et al. 2022).

A simple and widely used method for catalyst preparation is conventional chemical precipitation, which allows the formation of insoluble particles in a single-step process (Campanati et al. 2003). However, increasing attention has recently been directed toward an advanced synthesis technique, fluidized-bed homogeneous crystallization (FBHC). FBHC has been applied for the removal and recovery of various pollutants, including cations (Ni (Liao et al. 2024), Cu (Hsiao et al. 2023), Fe (Ha et al. 2025)) and anions (fluoride (Lacson et al. 2021), sulfide (Liao et al. 2022), phosphate (Ha et al. 2024, 2023, 2022)), as well as for water softening (Chou et al. 2024). This method offers several advantages, including simultaneous metal recovery, reduced waste generation, and more efficient pollutant separation. Importantly, the recovered metals are not only removed from wastewater but can also be valorized as catalysts in heterogeneous Fenton-like systems, thereby supporting circular economy strategies (Jiang et al. 2025).

Despite extensive research on persulfate-based advanced oxidation processes (AOPs) for dye degradation, several critical knowledge gaps remain. Most reported systems rely on Fe-based catalysts, which are limited by a narrow effective pH range, sludge generation, and potential secondary metal contamination. Although Fe-free catalysts have emerged as promising alternatives, investigations into bimetallic systems and their synergistic roles in persulfate activation remain limited. Moreover, catalyst synthesis has predominantly relied on conventional precipitation or hydrothermal methods, and the influence of synthesis strategy on catalytic performance has rarely been systematically examined. In addition, while fluidized-bed homogeneous crystallization (FBHC) has been widely applied for pollutant removal and metal recovery, the direct valorization of FBHC-derived materials as catalysts in sulfate-radical-based AOPs remains largely unexplored. To address these gaps, this study develops Ni–Cu bimetallic catalysts via jar-test precipitation and FBHC methods and evaluates their performance in sodium persulfate activation for the degradation of Reactive Black 5, thereby establishing a sustainable link between metal recovery and advanced oxidation processes.

Materials and methods

Materials

All chemicals were of analytical grade and used without further purification. Nickel(II) sulfate hexahydrate ($NiSO_4 \cdot 6H_2O$, Shimakyu Chemical Co., Ltd., Japan), copper(II) sulfate pentahydrate ($CuSO_4 \cdot 5H_2O$, Choneye, Taiwan), and anhydrous sodium carbonate (Na_2CO_3, United Chemical Works Co., Ltd., Taiwan) were used as metal precursors and as the precipitating agent for the synthesis of the Ni–Cu bimetallic catalyst. Sodium hydroxide (35% NaOH, Choneye, Taiwan) and sulfuric acid (95% H_2SO_4, Lien Hwa, Taiwan) were used to adjust the pH during catalyst synthesis and reaction experiments. Hydrogen peroxide (28% H_2O_2, Taoyuan, Taiwan) and sodium persulfate ($Na_2S_2O_8$, Hong Yao Chemical, Taiwan) were employed as oxidants. Reactive Black 5 (RB5, $C_{26}H_{21}N_5Na_4O_{19}S_6$, Maclin, Netherlands) was selected as the model azo dye. To identify the predominant reactive species involved in the degradation process, radical scavengers including tert-butanol (TBA), methanol (MeOH), furfuryl alcohol (FFA), and 1,4-benzoquinone (BQ) were employed. All solutions were prepared using reverse osmosis (RO) water produced in the laboratory using an RO purification system.

Ni–Cu catalyst synthesis

The Ni–Cu bimetallic catalyst was synthesized by two methods: conventional jar-test precipitation (JAR) and fluidized-bed homogeneous crystallization (FBHC).

Ni–Cu catalyst synthesis using JAR

For the precipitation method, the synthesis was conducted in a glass reactor (JAR, Fig. 1a) with a fixed Ni:Cu molar ratio of 1.08:1 and a metal-to-carbonate ratio of 1:1.75. Copper(II) sulfate pentahydrate ($CuSO_4·5H_2O$) and nickel(II) sulfate hexahydrate ($NiSO_4·6H_2O$) were dissolved in 1 L of deionized water under continuous stirring to ensure complete dissolution. The pH was adjusted and maintained at 7 throughout the synthesis, corresponding to the zeta potential near the isoelectric point (0 mV), which was identified as optimal for particle formation. An initial stirring rate of 150 rpm was applied for 10 min to uniformly disperse sodium carbonate (Na_2CO_3) and promote efficient reaction with the metal ions. The stirring speed was then reduced to 30 rpm and maintained for an additional 50 min to control particle growth and enhance crystallization, resulting in structurally stable precipitates. The pH was continuously monitored and adjusted when necessary. After synthesis, the particles were filtered and dried at 60 °C for 48–72 h.

Ni–Cu synthesis using FBHC

For the FBHC method (Fig. 1b), the catalyst was synthesized in a vertical fluidized-bed crystallization reactor with a total volume of 700 mL and a height of 108 cm, consisting of a straight cylindrical Section (80 cm) and a conical top Section (28 cm). The widened top section decreased the flow velocity and enhanced particle agglomeration by increasing collision frequency, thereby facilitating the growth of larger crystallites. The Ni–Cu and metal-to-carbonate molar ratios were the same as those used in the precipitation method (1.08:1 and 1:1.75, respectively). The synthesis solution containing Ni^{2+} and Cu^{2+} ions was prepared in a 30 L tank, while the carbonate precipitant solution was stored in a separate 30 L tank. Three peristaltic pumps were employed to control the input of the metal ion solution, the carbonate solution, and the internal recirculation flow. The pH of the reactor was continuously maintained at 7 throughout the 7-day synthesis period. After the reaction, the resulting particles were collected and dried at 60 °C for 48–72 h prior to use.

In a fluidized-bed reactor (FBR), crystallization is strongly influenced by hydrodynamics, particularly the recirculation flow rate (Q_R). A higher Q_R enhances ion dispersion and interparticle collisions, promoting uniform supersaturation and particle aggregation. Initially, homogeneous nucleation generates small $CuCO_3$ and $Ni_2(OH)_2CO_3·4H_2O$

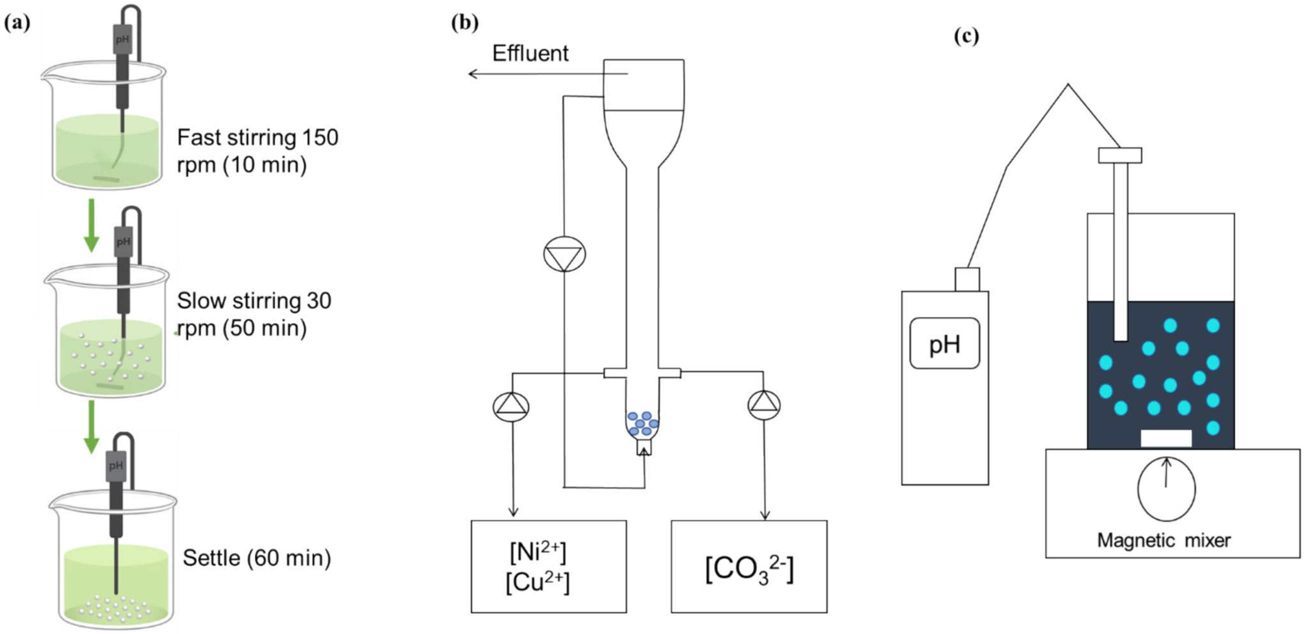

Fig. 1 Schematic of **a** JAR; **b** FBHC reactor for recovering Ni and Fe from wastewater and **c** Photo-Fenton-like system

precipitates from Ni, Cu, and CO_3^{2-} ions. These nuclei subsequently grow through secondary heterogeneous nucleation by attaching to existing solids and combining with newly formed precipitates, gradually enlarging the crystals. Continued growth and particle rearrangement transform dense clusters into larger, rounded granules. At elevated Q_R, repeated collisions and recrystallization lead to well-shaped, structurally stable particles with improved size uniformity. Similar hydrodynamic effects and crystallization behaviors have been reported in both modeling and experimental studies of fluidized-bed crystallization (Madlangbayan et al. 2025; Liu et al. 2024; Huang et al. 2024), supporting this mechanism.

Heterogeneous fenton-like degradation of RB5

The batch experiments were carried out in a 1 L glass beaker containing an initial RB5 concentration of 100 mg L^{-1} (Fig. 1c). The initial pH was adjusted between 3.0 and 8.0 using 1 N H_2SO_4 or 1 N NaOH. All experiments were conducted at ambient temperature (~22 °C). The catalyst dosage was varied from 0.2 to 1.0 g L^{-1}, and either hydrogen peroxide (H_2O_2) or sodium persulfate (SPS) was added as the oxidant. The solution was stirred at 300 rpm using a magnetic stirrer to ensure homogeneous mixing. Aliquots (5 mL) were withdrawn at predetermined intervals (0, 5, 10, 20, 30, 40, 50, and 60 min) using an automatic pipette. Each sample was diluted with 10 mL of deionized water, vortexed, and immediately filtered through a 0.22 µm membrane. The clear filtrate was then analyzed by UV–Vis spectrophotometry to evaluate the degree of decolorization.

The relative absorbance at time *t* was calculated using Eq. 1:

The discoloration of RB5 solutions was assessed by the relative absorbance decrease at 597 nm (λmax) (Chou et al. 2024):

$$\text{Relative absorbance (\%)} = \frac{Abs_t}{Abs_0} \tag{1}$$

where Abs_t is the absorbance for a given time t, and Abs_0 is the initial absorbance value.

Mineralization was evaluated by measuring total organic carbon (TOC) in the treated samples using a TOC analyzer. The percentage of TOC removal at a given reaction time was calculated:

$$\text{TOC removal (\%)} = \frac{TOC_0 - TOC_t}{TOC_0} \times 100 \tag{2}$$

where TOC_0 and TOC_t are the total organic carbon concentrations (mg L^{-1}) at time 0 and at time t, respectively.

Reaction kinetics were analyzed by assuming pseudo-first-order behavior with respect to dye concentration. For a first-order process, the absorbance decays exponentially so that (Domenzain-Gonzalez et al. 2021):

$$Ln\left(\frac{C_0}{C}\right) = k_{app}t \tag{3}$$

where C_0 is the initial concentration of the compound, C is the concentration at reaction time t, and kapp the total apparent velocity constant.

To investigate the role of adsorption and reactant concentration on the kinetics, we also examined the dependence of the apparent rate constant on the initial dye concentration $[RB5]_0$. Under the Langmuir–Hinshelwood (L–H) mechanism for heterogeneous catalysis, the surface reaction rate is given by a nonlinear expression (Eq. 4) (Afzal et al. 2025)

$$r_0 = \frac{K_C K_{ads}[RB5]_0}{1 + K_{ads}[RB5]_0} \tag{4}$$

where r_0 is the initial degradation rate (mg L^{-1} min^{-1}), K_C is the surface reaction rate constant (mg L^{-1} min^{-1}), and K_{ads} is the adsorption equilibrium constant (L mg^{-1}).

For experimental determination, Eq. 4 can be linearized into its double-reciprocal form (Eq. 5):

$$\frac{1}{r_0} = \frac{1}{K_C K_{ads}[RB5]_0} + \frac{1}{K_C}\cdot\frac{1}{[RB5]_0} \tag{5}$$

From the slope and intercept of the $1/r_0$ vs. $1/[RB5]_0$ plot, both K_C and K_{ads} can be determined, providing insight into adsorption and catalytic contributions to RB5 photocatalytic degradation (Khan et al. 2021).

Analytical methods

The physicochemical properties of the synthesized Ni–Cu catalysts and their performance in RB5 degradation were characterized using multiple analytical techniques. The crystalline structure of the catalyst was analyzed by X-ray diffraction (XRD, D8 Discover, Bruker Corp., Germany) within a 2θ range of 5°–90°. Surface functional groups were identified using Fourier-transform infrared spectroscopy (FT-IR, Nicolet 6700, Thermo Scientific, USA). X-ray photoelectron spectroscopy (XPS, Sigma Probe, Thermo VG Scientific, UK) was employed to determine the surface elemental composition and the oxidation states of Ni and Cu species. The surface morphology and particle size were examined by scanning electron microscopy (SEM, JEOL JSM-7800F, Japan), and elemental mapping was conducted using energy-dispersive X-ray spectroscopy (EDS). Zeta potential measurements were performed using a zeta potential analyzer (Zetasizer Nano ZS, Malvern Panalytical Ltd., UK) to determine the isoelectric point of the catalyst and to identify the optimal pH for the synthesis process. The leaching of Ni^{2+} and Cu^{2+} ions during the reaction was quantified by flame atomic absorption spectroscopy (FAAS, Analyst 500, PerkinElmer Corp., USA). RB5 decolorization was monitored by measuring the absorbance at 597 nm using a UV–Vis spectrophotometer (8453, Agilent Corp., USA). Mineralization efficiency was evaluated by total organic carbon (TOC) removal using a TOC analyzer (Aurora 1030, OI Analytical, USA). The identification of reactive oxygen species (ROS) involved in the degradation process was conducted via electron paramagnetic resonance (EPR/ESR) spectroscopy (JES-X310, JEOL, Japan). 5,5-Dimethyl-1-pyrroline-N-oxide (DMPO) and 2,2,6,6-tetramethylpiperidine (TEMP) were used as spin-trapping agents to detect ·OH, $SO_4^{\cdot -}$, $O_2^{\cdot -}$, and $^1O_2$ radicals.

Results and discussion

Characterization of Ni–Cu catalysts

The Ni–Cu bimetallic catalysts synthesized via conventional precipitation (JAR) and fluidized-bed homogeneous crystallization (FBHC) were characterized using XRD, FTIR, XPS, and SEM/EDS. Fourier-transform infrared (FTIR) spectroscopy (Fig. 2a) revealed the presence of hydroxyl (–OH) and carbonate (CO_3^{2-}) groups in both catalysts. A broad absorption band at ~ 3368 cm^{-1} (JAR) and ~ 3421 cm^{-1} (FBHC) was attributed to O–H stretching vibrations, with a stronger peak in the JAR catalyst, indicating higher water content. The bending vibrations of water molecules appeared at ~ 1635 cm^{-1} and were also more intense in the JAR

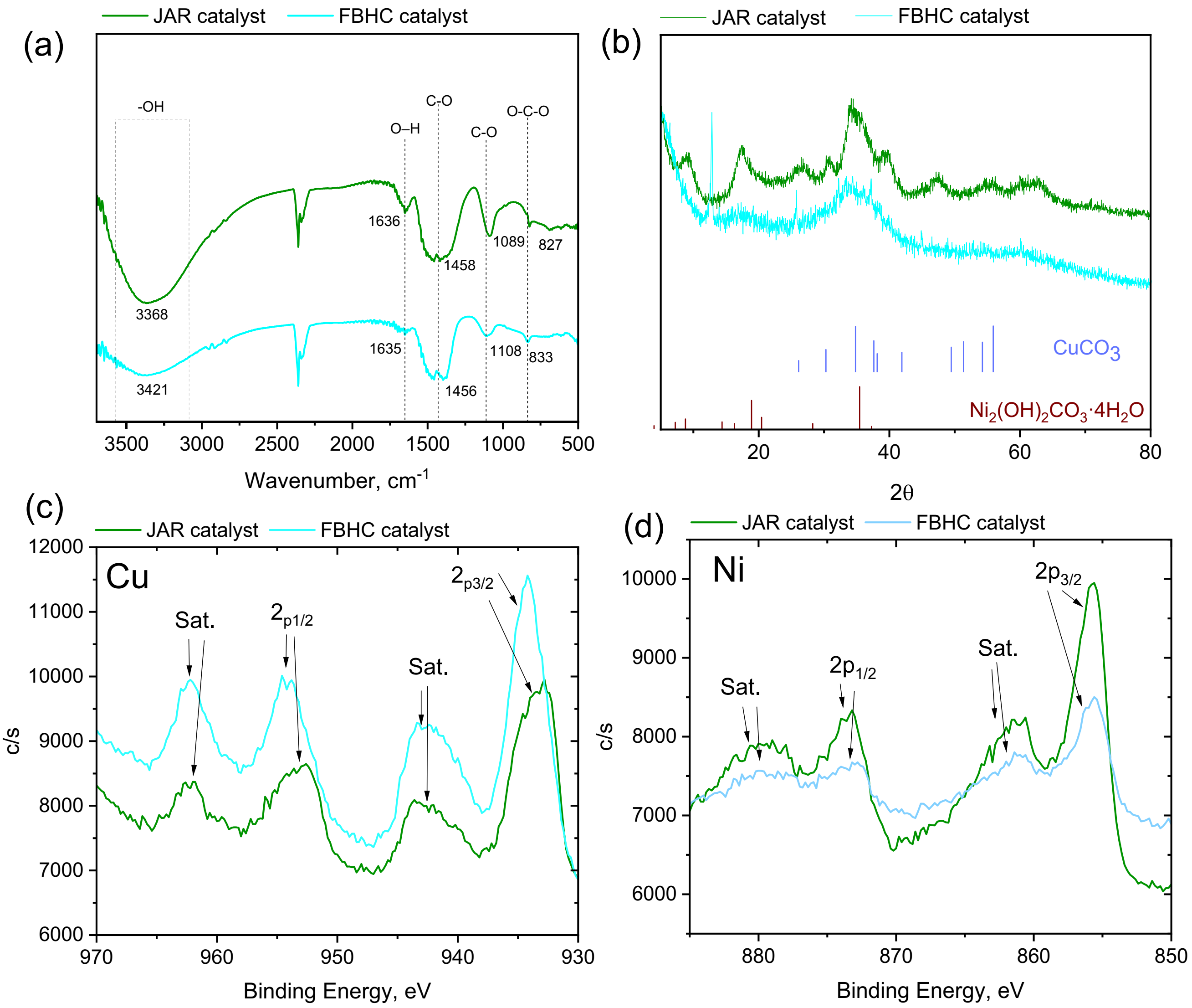

Fig. 2 Characterization of Ni–Cu catalysts (JAR vs. FBHC): **a** FTIR; **b** XRD; **c** Cu 2p XPS; **d** Ni 2p XPS

catalyst. In contrast, the FBHC-derived granules exhibited weaker O–H and H_2O-related signals, confirming their lower water content (Jiang et al. 2025; Liu et al. 2022; Valderama et al. 2025). Carbonate-related C–O stretching bands were identified at ~ 1456–1458 cm^{-1} and ~ 1089–1108 cm^{-1}, with a stronger band at ~ 1089 cm^{-1} in the JAR sample. Bands at ~ 827–833 cm^{-1} corresponded to O–C–O bending vibrations of carbonate groups (Shahid et al. 2018).

XRD analysis (Fig. 2b) revealed notable structural differences between the two catalysts. The JAR catalyst exhibited distinct and sharp diffraction peaks at $2\theta = 14.3°$, 27.5°, 30.8°, and 36.7°, corresponding to crystalline phases such as $CuCO_3$ and $Ni_2(OH)_2CO_3·4H_2O$. In contrast, the FBHC catalyst displayed broad and weak diffraction features, indicative of an amorphous structure. XPS analysis in Fig. 2c-d was used to examine surface chemical states and elemental composition. The Ni $2p_3/_2$ peak appeared at 855.7 eV for the JAR catalyst and 855.5 eV for the FBHC catalyst, with significantly higher intensity in the JAR sample, suggesting a higher nickel content. Satellite peaks in both spectra confirmed the presence of Ni^{2+} species (Abd El-Lateef et al. 2024). The Cu $2p_3/_2$ peaks were located at 932.9 eV (JAR) and 934.1 eV (FBHC), with the FBHC catalyst showing a more intense peak, indicating a higher copper concentration. Satellite peaks confirmed the presence of Cu(II) oxidation states (Conradie and Erasmus 2022). SEM results in Fig. 3 further revealed morphological differences between the catalysts. The JAR catalyst (Fig. 3a) exhibited a rough, irregular crystalline structure composed of sharp-edged particles, whereas the FBHC catalyst (Fig. 3b) demonstrated a more amorphous and porous morphology. At higher magnification (×30,000), the FBHC particles displayed a network of interconnected nanoscale grains, suggesting a higher specific surface area and greater availability of active sites for catalysis. EDS analysis confirmed distinct differences in elemental composition (Fig. 3c, d). The JAR sample contained higher levels of Cu (27.92%) and Ni (23.00%) but lower carbon content (8.31%), whereas the FBHC sample exhibited relatively lower Cu (23.13%) and Ni (17.80%) but significantly higher carbon content (18.24%). These compositional variations can be attributed to the distinct precipitation dynamics and ion incorporation mechanisms inherent to each synthesis method. Consistent with previous reports, FBHC-derived materials tend to display improved crystal uniformity, structural stability, and selective element incorporation compared with batch-precipitated counterparts, owing to enhanced mass transfer and localized supersaturation during the crystallization process (Huang et al. 2024).

Catalyst from JAR and FBHC comparison

To better understand the catalytic performance of the two synthesis methods, kinetic analysis was conducted to compare the degradation rates of RB5 using JAR- and FBHC-derived catalysts. While RB5 removal efficiency (Fig. 4a) suggested faster decolorization with FBHC, quantifying the reaction kinetics (Fig. 4b) through pseudo-first-order rate constants provides a more rigorous evaluation of catalyst activity.

The catalytic performance of the FBHC-derived material was consistently superior to that of the JAR catalyst. As shown in Fig. 4a, RB5 removal with FBHC proceeded much faster, achieving almost complete decolorization (< 5% residual RB5) within 60 min, whereas the JAR catalyst required the same period to reach only ~ 4–5% removal, with slower decolorization even at longer times. Correspondingly, TOC removal stabilized at 29% for FBHC, reflecting rapid initial mineralization within the first 5–10 min, while the JAR catalyst achieved only 25% removal after 60 min. These results indicate that FBHC not only accelerates dye degradation but also enhances early-stage mineralization of organic carbon.

Kinetic analysis (Fig. 4b) further confirmed the superior catalytic activity of the FBHC material. The

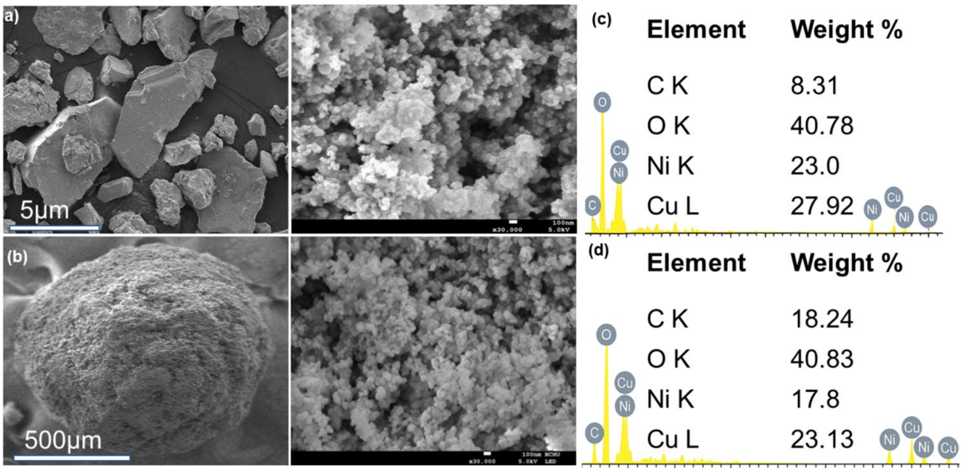

(c)

Element	Weight %
C K	8.31
O K	40.78
Ni K	23.0
Cu L	27.92

(d)

Element	Weight %
C K	18.24
O K	40.83
Ni K	17.8
Cu L	23.13

Fig. 3 SEM images of Ni–Cu catalysts: **a** ×5,000 JAR; **b** ×5,000 FBHC; EDS analysis of **c** JAR and **d** FBHC

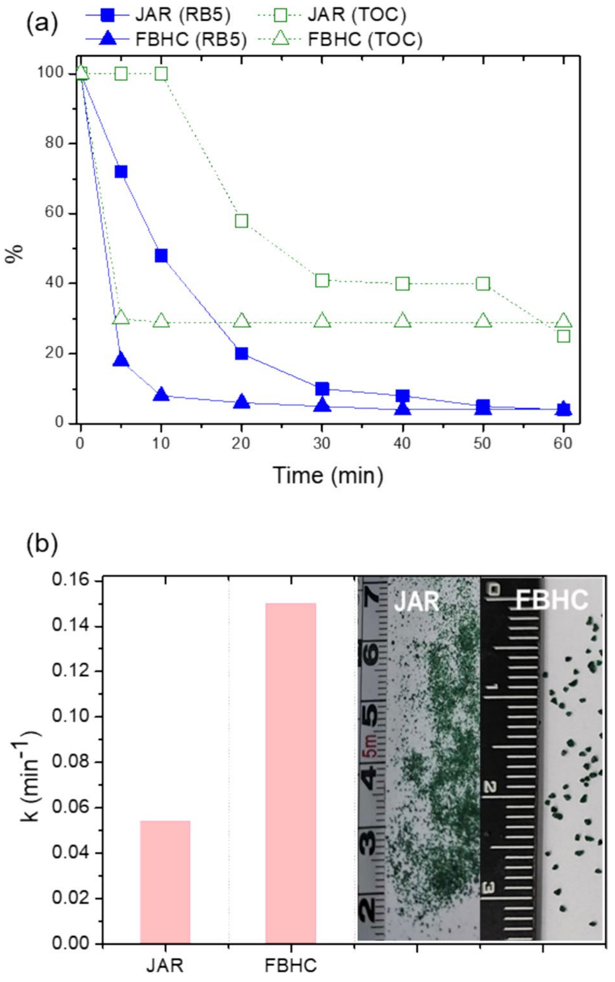

Fig. 4 **a** Effect of RB5 and TOC removal, and **b** kinetic rate constants using catalysts derived from JAR and FBHC

pseudo-first-order rate constant (k) for RB5 removal using the FBHC catalyst was 0.150 min^{-1}, nearly three times higher than that of the JAR catalyst (0.054 min^{-1}). This substantial enhancement in reaction kinetics demonstrates that FBHC promotes much faster pollutant degradation, consistent with the rapid RB5 decolorization observed in Fig. 4a. The improved rate constant can be attributed to the larger, uniformly shaped granules produced by FBHC, which provide better surface accessibility and reduce particle agglomeration compared with the fine, irregular particles obtained from JAR (Jiang et al. 2025; Keselytė et al. 2025). These structural advantages not only accelerate the degradation reaction but also improve catalyst stability and facilitate recovery, highlighting the practical benefits of the FBHC synthesis method. Overall, the superior performance of the FBHC-derived catalyst demonstrates its potential for use in further experiments.

Role of pH and oxidant in RB5 decolorization

The initial pH of the reaction medium strongly influences the ionization state of RB5, the surface charge of the catalyst, and the oxidation potential of reactive radicals, making it a critical parameter in catalytic processes (Alhamd et al. 2021). In addition, catalytic efficiency depends not only on the catalyst type but also on the oxidant employed (Javaid and Qazi 2019).

As shown in Fig. 5a, RB5 decolorization was evaluated at different initial pH values (3.0, 5.0, 6.5, and 8.0) across several systems: catalyst only, oxidant only (H_2O_2 or SPS), and catalyst combined with oxidant. The Ni–Cu catalyst alone achieved limited removal (11.9–25.8%) at all pH values, indicating weak adsorption capacity. Similarly, H_2O_2 or SPS without catalyst produced noticeable decolorization only at pH 3.0 (19.3 and 25.7%, respectively), while removal dropped to < 2% under neutral and alkaline conditions, confirming that both oxidants are ineffective without catalytic activation.

In contrast, coupling the catalyst with an oxidant significantly enhanced RB5 degradation. The catalyst + H_2O_2 system removed ~ 69.7% of RB5 at pH 3.0, but performance declined sharply to ~ 21.1% at pH 5.0 and ~ 17–19% at pH 6.5–8.0. The catalyst + SPS system, however, exhibited consistently high efficiency across the entire pH range, achieving ~ 95.2% removal at pH 3.0, ~ 90.5% at pH 6.5, and ~ 87.5% at pH 8.0. This superior performance is attributed to the generation of sulfate radicals ($SO_4\cdot^-$), which are more stable and active across a wider pH range than hydroxyl radicals (·OH) derived from H_2O_2. At higher pH, however, excess OH^- can quench $SO_4\cdot^-$, converting them into less reactive ·OH radicals and causing a slight decline in efficiency (Javaid and Qazi 2019).

Metal leaching, shown in Fig. 5**b,** was also strongly pH-dependent. At pH 3.0, the catalyst released ~ 3.56 mg/L Ni and ~ 2.04 mg/L Cu due to acid-induced dissolution. Leaching decreased with increasing pH: ~ 2.72 mg/L Ni and 1.12 mg/L Cu at pH 5.0, ~ 2.1 mg/L Ni and 1.1 mg/L Cu at pH 6.5, and minimal values (~ 1.34 mg/L Ni and 0.57 mg/L Cu) at pH 8.0. Although maximum RB5 removal occurred at pH 3.0, practical applications favor near-neutral conditions. At pH 6.5, the catalyst + SPS system still achieved ~ 90.5% decolorization while greatly reducing metal leaching. Notably, the Cu leaching concentration at this pH (~ 1.1 mg/L) is below the Taiwan effluent standard of 1.5 mg/L, minimizing secondary contamination. Moreover, operating near pH 6–7 aligns with typical textile wastewater conditions, avoiding the need for additional acidification or neutralization (Castillo-Suárez et al. 2023).

Therefore, pH 6.5 represents an optimal compromise, providing high catalytic activity, reduced metal leaching, and practical feasibility. These results demonstrate that persulfate-activated Ni–Cu catalysis is effective over a broad pH range, with neutral to slightly acidic conditions offering the best balance of efficiency and stability.

Catalyst type, particle size, and operational effects on RB5 removal

The catalytic degradation of RB5 in persulfate-based advanced oxidation processes is strongly influenced by both the physicochemical properties of the catalyst and the operational parameters of the reaction system. Key factors include catalyst particle size (Mbarek et al. 2023), dosage (Rashtbari et al. 2023), and oxidant (SPS) concentration (Wu et al. 2022), which govern the availability of active sites, the rate of reactive oxygen species generation, and overall reaction kinetics (Alhamd et al. 2021). Moreover, the catalyst synthesis method can significantly affect structural properties such as crystallinity, surface area, and porosity, which in turn dictate catalytic performance (Yamanaka and Shimazu 2022).

Catalyst particle size had a pronounced impact on RB5 removal. When ground to a fine fraction (≤ 0.053 mm), the initial decolorization rate and overall removal efficiency increased substantially due to a larger external surface area and shorter diffusion paths, which expose more active sites for persulfate activation and dye adsorption. Fine-particle catalysts consistently achieved higher decolorization within the same reaction time compared with coarser pellets (Santos et al. 2015; Liang et al. 2025).

Figure 6a presents a contour map of RB5 decolorization (%) as a function of catalyst dosage and SPS concentration. Maximum conversion (> 90%) was observed at 0.5 g L^{-1} catalyst and 6.25 mM SPS. Increasing catalyst loading from 0.2 to 0.5 g L^{-1} markedly accelerated decolorization, whereas further increases to 1.0 g L^{-1} provided no additional improvement, consistent with literature reports of mass-transfer limitations and unproductive oxidant consumption at excessive catalyst loadings (Rezaei et al. 2023). Similarly, increasing SPS concentration enhanced reaction kinetics: plots of $\ln(ABS_0/ABS_t)$ versus time (Fig. 6d) were linear, indicating pseudo-first-order behavior, with the apparent rate constant (k_{app}) increasing from ~ 0.0037 to 0.0554 min^{-1} as SPS concentration increased from 0 to 6.25 mM, and the corresponding half-life ($t_{1/2}$) decreasing from ≈187.3 to ≈12.5 min (Fig. 6c). These trends confirm that higher persulfate availability promotes $SO_4\cdot^-$ generation and accelerates RB5 degradation, consistent with previous observations that oxidant dosage enhances dye removal up to an optimum before radical scavenging becomes significant (Rambu et al. 2018). Taken together, the kinetic data (Fig. 6b–d) indicate that practical optimum conditions are achieved using fine particles, ~ 0.5 g L^{-1} catalyst, and ~ 6.25 mM SPS.

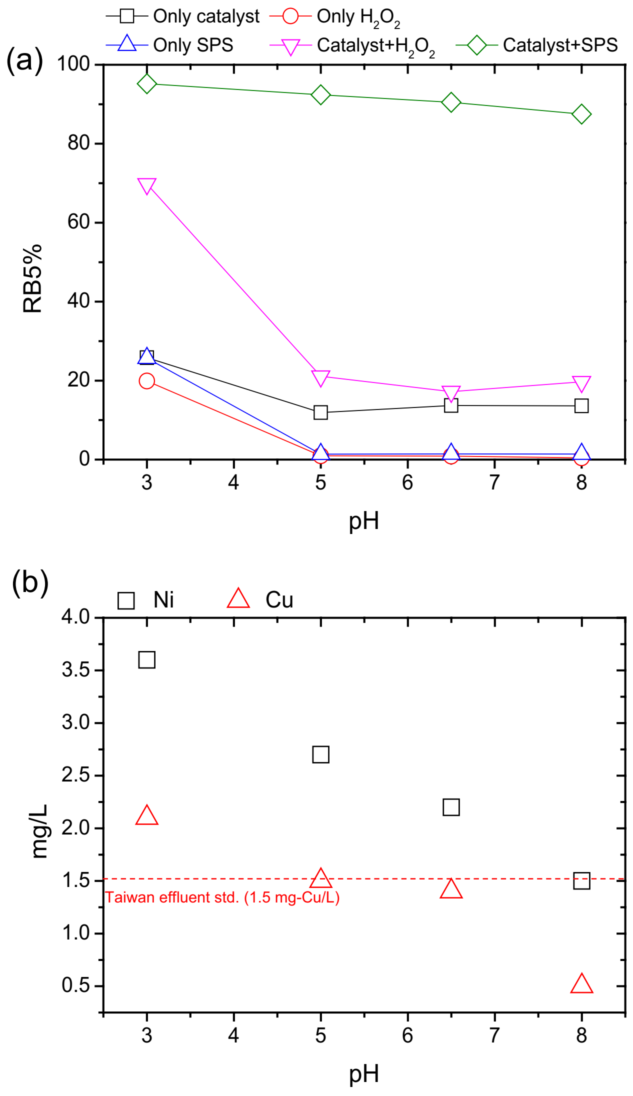

Fig. 5 **a** RB5 removal (%) after 60 min at different initial pH (3–8) for Ni–Cu only (0.5 g/L), H_2O_2 only (7.633 mM), SPS only (6.25 mM), catalyst + H_2O_2, and catalyst + SPS; **b** Ni^{2+} and Cu^{2+} leaching (mg/L) after 60 min versus pH

Beyond particle size, catalyst loading, and oxidant concentration, the synthesis method critically influences the structural and surface characteristics of Ni–Cu catalysts, directly affecting their activity in RB5 degradation (Yamanaka and Shimazu 2022). To eliminate particle size distribution effects and better reflect industrially relevant conditions, both catalysts were ground to fine powder prior to evaluation. Under identical reaction conditions, the FBHC catalyst clearly outperformed the JAR catalyst, achieving > 80% RB5 decolorization within 5 min and 94% after 10 min, whereas the JAR catalyst removed only 28% within 5 min and required 40 min to reach 90% decolorization. Total organic carbon (TOC) removal followed a similar trend: the FBHC catalyst achieved 70.7% reduction within 5 min and remained stable, while the JAR catalyst reached only 59.9% after 20 min.

The superior activity of the FBHC catalyst is attributed to its larger specific surface area, as SEM images revealed a more irregular and textured surface compared with the JAR catalyst. Crystallinity also plays a key role: XRD analysis demonstrated that the FBHC catalyst possesses an amorphous structure, whereas the JAR catalyst is more crystalline. Amorphous carbonates enhance reaction rates due to their higher surface area and greater density of defect-rich active sites, which facilitate metal ion release and interaction with oxidants (Cai et al. 2020; Yu et al. 2024). Additional advantages of the FBHC catalyst include lower residual moisture and higher crystal purity, further improving catalytic performance and structural stability (Mahasti et al. 2022). Overall, amorphous catalysts with high surface area and abundant reactive sites generally exhibit superior reactivity and faster degradation of organic pollutants compared with well-crystallized catalysts (Zhu et al. 2023b).

Adsorption and reactive radical contributions

The significance of surface interactions in heterogeneous Fenton-like reactions was evaluated through kinetic analysis using the Langmuir–Hinshelwood (L–H) model (Fig. 7). Because oxidation occurs primarily on the catalyst surface (Hu et al. 2020), adsorption plays a critical role in controlling degradation efficiency. As shown in Fig. 7a, RB5 removal decreased with increasing initial dye concentration: faster decolorization was observed at lower concentrations (20–50 mg/L), whereas higher concentrations (200–400 mg/L) exhibited slower rates, reflecting limitations in available surface sites. A strong linear correlation between $1/k_{app}$ and initial RB5 concentration ($R^2 = 0.9697$, Fig. 7b) confirmed L–H-type kinetics, indicating that surface adsorption was the rate-limiting step. The high Kc value (9.61 mg/(L·min)) suggested that adsorbed RB5 molecules were readily available for attack by reactive species such as

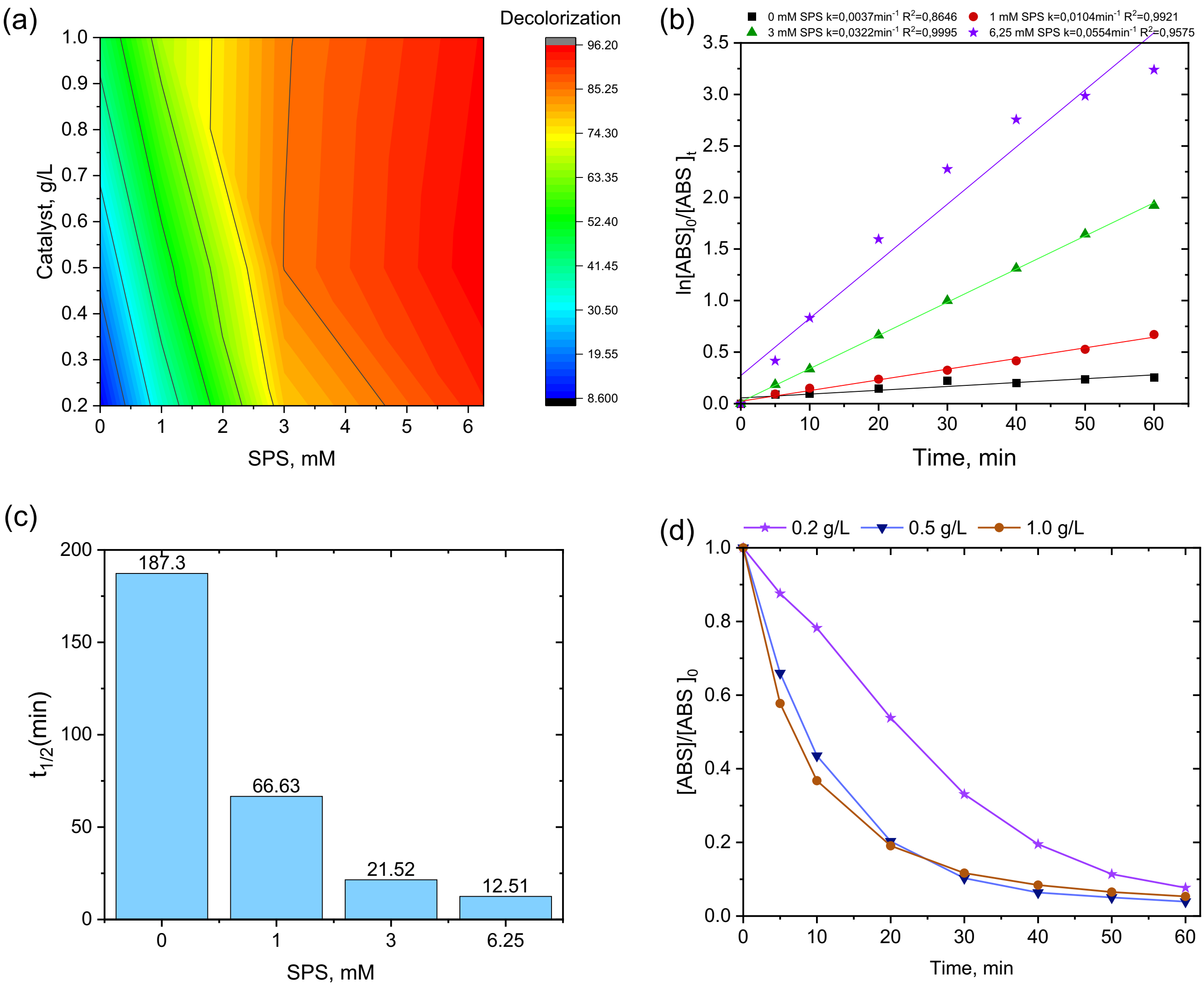

Fig. 6 Effect of SPS concentration and catalyst dose on RB5 decolorization: **a** 60 min removal efficiency; **b** pseudo-first-order kinetics at varying SPS; **c** RB5 half-life vs. SPS; **d** degradation profiles at different catalyst dosages

sulfate ($SO_4^{\cdot-}$) and hydroxyl ($\cdot OH$) radicals. In contrast, the low K_ad_s value (0.0169 L/mg) indicated limited adsorption capacity, leading to reduced reaction rates at higher dye concentrations. These findings underscore the critical role of surface interactions: reactive oxygen species preferentially attack adsorbed dye molecules, while higher RB5 concentrations saturate the surface and reduce overall degradation efficiency, which may also suppress electron–hole recombination and enhance catalytic performance (Khan et al. 2021).

To identify the reactive oxygen species (ROS) involved, selective scavengers were employed based on known reaction rate constants. Methanol, which reacts rapidly with both $\cdot OH$ ($k=9.7\times10^8\ M^{-1}\ s^{-1}$) and $SO_4^{\cdot-}$ ($k=2.5\times10^7\ M^{-1}\ s^{-1}$), served as a non-selective radical quencher. Tert-butanol (TBA), reacting primarily with $\cdot OH$ ($k=3.8$–$7.6\times10^8\ M^{-1}\ s^{-1}$) but poorly with $SO_4^{\cdot-}$ ($k=4$–$9.5\times10^5\ M^{-1}\ s^{-1}$), was used as a selective $\cdot OH$ scavenger (Hu et al. 2020). In the Ni–Cu + SPS system, baseline RB5 removal was ~ 96%. Addition of furfuryl alcohol (FFA, 0.02 M), a selective $^1O_2$ scavenger, decreased removal to 66.7%, indicating that ~ 30% of degradation was mediated by $^1O_2$. TBA (1 M) reduced removal to ~ 81%, suggesting that $\cdot OH$ contributed partially (~ 15%) but was not dominant. Methanol (1 M) caused a larger decrease to 42.9%, confirming that radical species—particularly $SO_4^{\cdot-}$—were the primary oxidants. Finally, p-benzoquinone (BQ, 0.01 M), a selective $O_2^{\cdot-}$ scavenger ($k=2.9\times10^9\ M^{-1}\cdot s^{-1}$) (Wang et al. 2022), caused only a slight decrease (~ 4%), indicating negligible involvement of $O_2^{\cdot-}$ (Fig. 8a). Overall, the ROS contribution in the Ni–Cu + SPS system followed the order: $SO_4^{\cdot-} > {}^1O_2 > \cdot OH > O_2^{\cdot-}$ (Fig. 8b–d). By contrast, the Ni–Cu + H_2O_2 system exhibited low activity (~ 22% RB5 removal). Scavenger tests revealed that only $O_2^{\cdot-}$ was significant: BQ reduced removal to ~ 15.8% (~ 6.4% drop), whereas MeOH, TBA, and FFA caused minor decreases (~ 1–2%), indicating minimal generation of $\cdot OH$ and $^1O_2$. These results demonstrate that under these conditions, H_2O_2 activation on Ni–Cu primarily produces transient $O_2^{\cdot-}$, resulting in poor overall degradation.

EPR spin-trapping experiments corroborated the scavenger test results. DMPO/H_2O was employed to detect $\cdot OH$ and $SO_4^{\cdot-}$, DMPO/MeOH for $O_2^{\cdot-}$, and TEMP/MeOH for $^1O_2$ (Chen et al. 2022). The DMPO–$O_2^{\cdot-}$ adduct exhibited a characteristic 2:2:1:2:1:2 intensity ratio, whereas DMPO–$SO_4^{\cdot-}$ and DMPO–$\cdot OH$ adducts produced 1:1:1:1:1:1 and 1:2:2:1 multiplets, respectively (Sarkar et al. 2022). In the Ni–Cu + SPS system, DMPO/H_2O spectra showed a mixed $\cdot OH/SO_4^{\cdot-}$ signal (1:1:1:1:1:1 for $SO_4^{\cdot-}$; 1:2:2:1 for $\cdot OH$) with strong intensity throughout 60 min. TEMP–$^1O_2$ triplets appeared almost immediately and remained stable, while DMPO/MeOH revealed a weaker DMPO–$O_2^{\cdot-}$ sextet. These results confirm continuous generation of $SO_4^{\cdot-}$, $\cdot OH$, and sustained $^1O_2$ production. By contrast, EPR signals in the Ni–Cu + H_2O_2 system were weak and transient: a brief DMPO–$O_2^{\cdot-}$ signal appeared at 1 min and quickly disappeared, a faint DMPO–$\cdot OH$ signal was observed only at early times, and no TEMP–$^1O_2$ signal was detected. These observations align with scavenger experiments, indicating that Ni–Cu + SPS produces multiple ROS with $SO_4^{\cdot-}$ and $^1O_2$ dominant, whereas Ni–Cu + H_2O_2 primarily generates short-lived $O_2^{\cdot-}$.

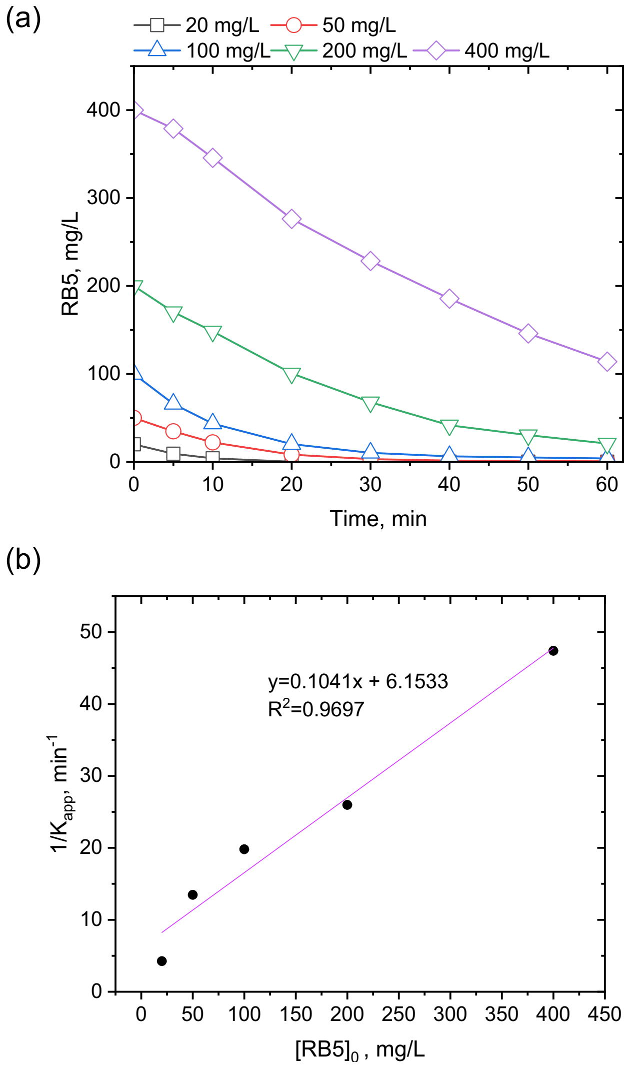

Fig. 7 **a** Effect of initial RB5 concentration, and **b** Langmuir–Hinshelwood plot for RB5 degradation

The catalytic degradation of RB5 proceeds via surface-mediated activation of persulfate ($S_2O_8^{2-}$) and peroxymonosulfate (HSO_5^-) at ≡Cu(II) and ≡Ni(II) sites, generating sulfate radicals ($SO_4^{\cdot-}$) and peroxymonosulfate radicals ($SO_5^{\cdot-}$). These primary radicals subsequently undergo transformations in aqueous solution to produce secondary reactive oxygen species, including hydroxyl radicals ($\cdot OH$), superoxide ($O_2^{\cdot-}$), and singlet oxygen ($^1O_2$). Concurrent electron transfer between Cu^+/Cu^{2+} and Ni^{2+}/Ni^{3+} maintains continuous redox cycling, thereby sustaining oxidant activation. The coexistence and interconversion of radical and non-radical species establish a mixed oxidation system at the catalyst–solution interface.

The process is initiated by hydrolysis and ionization of persulfate and peroxymonosulfate, producing reactive precursor species (Tian et al. 2022; Lee et al. 2018):

$$S_2O_8^{2-} + H_2O \rightarrow HSO_5^- + HSO_4^- \tag{6}$$

$$HSO_5^- \rightarrow H^+ + SO_5^{2-} \tag{7}$$

$$HSO_4^- \rightarrow H^+ + SO_4^{2-} \tag{8}$$

Surface-bound metals, particularly Cu(I) and Ni(II), activate persulfate and peroxymonosulfate to produce radicals (Tian et al. 2021; Ding et al. 2022):

$$\equiv M^n + S_2O_8^{2-} \rightarrow \cdot SO_4^- + SO_4^{2-} + M^{n+1} \tag{9}$$

Redox cycling of the metal sites is maintained via electron transfer:

$$\equiv Ni^{3+} + Cu^+ \rightarrow Ni^{2+} + Cu^{2+} \tag{10}$$

$$\equiv Cu^+ + Ni^{3+} \rightarrow Cu^{2+} + Ni^{2+} \tag{11}$$

The generated radicals interconvert in aqueous solution, producing additional ROS (Zhu et al. 2018):

$$\cdot SO_4^- + H_2O \rightarrow SO_4^{2-} + \cdot OH + H^+ \tag{12}$$

$$SO_4^{2-} + \cdot OH + H^+ \rightarrow H_2O + \cdot SO_4^- \tag{13}$$

$$SO_5^{2-} + H_2O \rightarrow \cdot O_2^- + SO_4^{2-} + H^+ \tag{14}$$

$$\cdot SO_5^- + \cdot SO_5^- \rightarrow S_2O_8^{2-} + {}^1O_2 \tag{15}$$

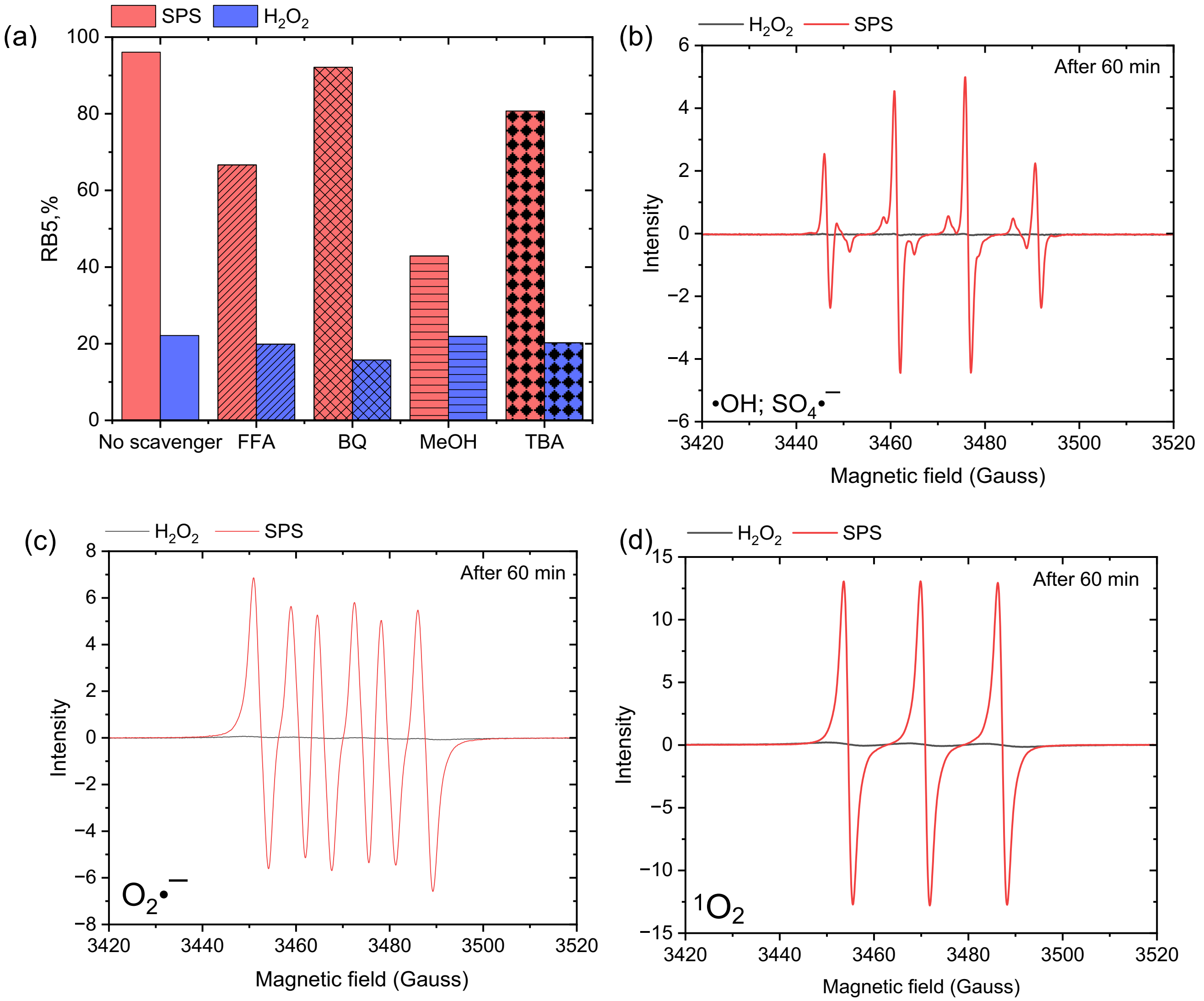

Fig. 8 **a** Radical scavenging experiment; ESR signals for **b** $\cdot OH/SO_4\cdot^-$, **c** $O_2\cdot^-$, and **d** $^1O_2$

$$\cdot 2O_2^{-} + 2H_2O \rightarrow H_2O_2 + {}^1O_2 + 2OH^{-} \quad (16)$$

$$S_2O_8^{2-} + \cdot O_2^{-} \rightarrow \cdot SO_4^{-} + SO_4^{2-} + O_2 \quad (17)$$

$$\cdot OH + \cdot SO_4^{-} \rightarrow HSO_5^{-} \quad (18)$$

Most of the currently available literature considered that the possibility of formation of $CO_3^{\cdot-}$ is through reactions of $HO^{\cdot}$ with HCO_3^{-}/CO_3^{2-} (Sharma et al. 2025):

$$HCO_3^{-} + \cdot OH \rightarrow \cdot CO_3^{-} + H_2O \quad (19)$$

$$CO_3^{2-} + \cdot OH \rightarrow \cdot CO_3^{-} + OH^{-} \quad (20)$$

Ultimately, the active species ($\cdot OH$, $SO_4^{\cdot-}$, $CO_3^{\cdot-}$, $^1O_2$, and $\cdot O_2^{-}$) react with RB5, resulting in its rapid mineralization to CO_2, H_2O, and mineral acids:

$$\cdot OH, \cdot SO_4^{-}, \cdot CO_3^{-}, {}^1O_2, \text{ and } \cdot O_2 + RB5 \rightarrow H_2O + CO_2 + \text{mineral acids} \quad (21)$$

Conclusion

This study demonstrated the efficient degradation of Reactive Black 5 (RB5) using Ni–Cu bimetallic catalysts synthesized via conventional precipitation (JAR) and fluidized-bed homogeneous crystallization (FBHC). The JAR catalyst exhibited limited activity, requiring over 40 min to reach 90% decolorization and achieving only 59.9% TOC removal after 20 min. In contrast, the FBHC catalyst achieved > 90% color removal within 10 min and rapid mineralization, reaching 70.7% TOC reduction after just 5 min. Kinetic analysis confirmed that degradation followed the Langmuir–Hinshelwood model, with surface adsorption as a key step. Radical scavenger experiments and EPR measurements revealed that $SO_4^{\cdot-}$ and $^1O_2$ were the dominant reactive oxygen species in the SPS-based system, while ·OH contributed partially and $O_2^{\cdot-}$ was negligible. H_2O_2 activation on Ni–Cu primarily generated transient $O_2^{\cdot-}$, resulting in low degradation efficiency. Overall, the FBHC-synthesized catalyst not only outperformed the JAR material but also exhibited rapid mineralization and stable activity under near-neutral pH, overcoming key limitations of conventional Fenton-like systems. These findings highlight the potential of Ni–Cu/SPS systems as a promising Fe-free advanced oxidation process for textile wastewater treatment. However, this study was conducted using a model dye under laboratory conditions; validation with real textile effluents is needed. A systematic investigation of catalyst regeneration using chemical eluents was beyond the scope of this study and will be addressed in future work. Further investigations should address long-term catalyst stability, metal leaching, and the mechanistic role of Ni–Cu synergy. In addition, identification of degradation intermediates via GC–MS analysis is recommended to elucidate reaction pathways, assess potential toxicity, and support pilot-scale evaluation for practical applications.

Acknowledgements The authors gratefully acknowledge the technical support for SEM, XRD, and XPS measurements provided by the Instrument Center of National Chung Hsing University, Taiwan.

Funding Open access funding provided by National Chung Hsing University. This work was financially supported by the National Science and Technology Council, Taiwan (under Contract Number NSTC 114-2221-E-005-013-MY3) and the Innovation and Development Center of Sustainable Agriculture from the Featured Areas Research Center Program, within the framework of the Higher Education Sprout Project by the Ministry of Education, Taiwan. The study was also supported by the Taiwan Experience Education Program (TEEP), Ministry of Education, Taiwan.

Declarations

Conflict of interest The authors declare that they have no conflict of interest.

References

Abd El-Lateef HM, Khalaf MM, Mohamed IM (2024) XPS analysis, voltammetric, and impedance characteristics of novel heterogeneous biphosphates based on Cu/Ni for tri (ammonium) phosphate oxidation: a new direction for material processing in fuel technology. Fuel 356:129618. https://doi.org/10.1016/j.fuel.2023.129618

Afzal MY, Bilal M, Khan H, Asif M, Khan MS, Iqbal M, Butt TA, Hassan M, Shaikh AJ (2025) Understanding photocatalytic degradation of RB5 dye under salts using nickel sulfide nanoparticles: insights from dynamic light scattering and theoretical investigations. ACS Omega 10(30):32918–32938. https://doi.org/10.1021/acsomega.5c01902

Alhamd M, Tabatabaie T, Parseh I, Amiri F, Mengelizadeh N (2021) Magnetic CuNiFe2O4 nanoparticles loaded on multi-walled carbon nanotubes as a novel catalyst for peroxymonosulfate activation and degradation of Reactive Black 5. Environ Sci Pollut Res 28(40):57099–57114. https://doi.org/10.1007/s11356-021-14590-2

Anthony P, Doğan Ş (2023) Degradation of reactive black 5 by ultrasound-activated persulfate process: kinetics, mineralization, and by-products. Desalin Water Treat 285:298–304. https://doi.org/10.5004/dwt.2023.29317

Cai W, Chen R, Yang H, Tao HB, Wang HY, Gao J, Liu W, Liu S, Hung SF, Liu B (2020) Amorphous versus crystalline in water oxidation catalysis: a case study of NiFe alloy. Nano Lett 20(6):4278–4285. https://doi.org/10.1021/acs.nanolett.0c00840

Campanati M, Fornasari G, Vaccari A (2003) Fundamentals in the preparation of heterogeneous catalysts. Catal Today 77(4):299–314. https://doi.org/10.1016/S0920-5861(02)00375-9

Castillo-Suárez LA, Sierra-Sánchez AG, Linares-Hernández I, Martínez-Miranda V, Teutli-Sequeira EA (2023) A critical review of textile industry wastewater: green technologies for the removal of indigo dyes. Int J Environ Sci Technol 20(9):10553–10590. https://doi.org/10.1007/s13762-023-04810-2

Chen L, Duan J, Du P, Sun W, Lai B, Liu W (2022) Accurate identification of radicals by in-situ electron paramagnetic resonance in ultraviolet-based homogenous advanced oxidation processes. Water Res 221:118747. https://doi.org/10.1016/j.watres.2022.118747

Chou YC, Ha TH, Lu MC (2024) Optimum operation condition of fluidized-bed homogeneous crystallization technology for the recovery of carbon dioxide captured in flue gas. J Environ Chem Eng 12(3):112943. https://doi.org/10.1016/j.jece.2024.112943

Conradie J, Erasmus E (2022) XPS photoelectron lines, satellite structures and Wagner plot of Cu (II) β-diketonato complexes explained in terms of its electronic environment. J Electron Spectrosc Relat Phenom 259:147241. https://doi.org/10.1016/j.elspec.2022.147241

da Silva ÉF, Ximenes ÉR, de Sales LB, Dantas EJ, Oliveira ED, Simões TB, Ribeiro AT, Sanz O, Machado G, Almeida LC (2022) Photocatalytic degradation of RB5 textile dye using immobilized TiO2 in brass structured systems. Catal Today 383:173–182. https://doi.org/10.1016/j.cattod.2021.02.006

Ding Y, Fu L, Peng X, Lei M, Wang C, Jiang J (2022) Copper catalysts for radical and nonradical persulfate based advanced oxidation processes: certainties and uncertainties. Chem Eng J 427:131776. https://doi.org/10.1016/j.cej.2021.131776

Domenzain-Gonzalez J, Castro-Arellano JJ, Galicia-Luna LA, Rodriguez-Cruz M, Hernandez-Lopez RT, Lartundo-Rojas L (2021) Photocatalytic membrane reactor based on Mexican natural zeolite: RB5 dye removal by photo-Fenton process. J Environ Chem Eng 9(4):105281. https://doi.org/10.1016/j.jece.2021.105281

Fadaei S, Noorisepehr M, Pourzamani H, Salari M, Moradnia M, Darvishmotevalli M, Mengelizadeh N (2021) Heterogeneous activation of peroxymonosulfate with Fe3O4 magnetic nanoparticles for degradation of Reactive Black 5: batch and column study. J Environ Chem Eng 9(4):105414. https://doi.org/10.1016/j.jece.2021.105414

Gul R, Sharma P, Kumar R, Umar A, Ibrahim AA, Alhamami MA, Jaswal VS, Kumar M, Dixit A, Baskoutas S (2023) A sustainable approach to the degradation of dyes by fungal species isolated from industrial wastewaters: performance, parametric optimization, kinetics and degradation mechanism. Environ Res 216:114407. https://doi.org/10.1016/j.envres.2022.114407

Ha TH, Mahasti NN, Lu MC, Huang YH (2022) Application of low-solubility dolomite as seed material for phosphorus recovery from synthetic wastewater using fluidized-bed crystallization (FBC) technology. Sep Purif Technol 303:122192. https://doi.org/10.1016/j.seppur.2022.122192

Ha TH, Mahasti NNN, Lin CS, Lu MC, Huang YH (2023) Enhanced struvite (MgNH4PO4· 6H$_2$O) granulation and separation from synthetic wastewater using fluidized-bed crystallization (FBC) technology. J Water Process Eng 53:103855. https://doi.org/10.1016/j.jwpe.2023.103855

Ha TH, Mahasti NN, Ha HQ, Liao PL, Huang YH, Lu MC (2024) Recovery of nitrogen as struvite from swine wastewater: comparison study of batch and continuous fluidized-bed crystallization process. Sep Purif Technol 351:128045. https://doi.org/10.1016/j.seppur.2024.128045

Ha TH, Huang YH, Lu MC (2025) Chemical precipitation processes valorizing two waste streams amalgamating Fe-rich welding wastewater and P-rich swine slurry leachate into FePO4. J Clean Prod 488:144632. https://doi.org/10.1016/j.jclepro.2024.144632

Han B, Shu D, Cao S, Lian Z, An F, Li W, Bai S (2024) Role of surfactants in the degradation and sustainable dyeing for reactive dyeing wastewater. J Mol Liq 410:125657. https://doi.org/10.1016/j.molliq.2024.125657

Hsiao CT, Huang TH, Lacson CFZ, Vilando AC, Lu MC (2023) Recovering struvite from livestock wastewater by fluidized-bed homogeneous crystallization as a pre-treatment process to sludge co-digestion. Environ Res 235:116639. https://doi.org/10.1016/j.envres.2023.116639

Hu J, Zeng X, Yin Y, Liu Y, Li Y, Hu X, Zhang L, Zhang X (2020) Accelerated alkaline activation of peroxydisulfate by reduced rubidium tungstate nanorods for enhanced degradation of Bisphenol A. Environ Sci Nano 7(11):3547–3556. https://doi.org/10.1039/D0EN00840K

Huang PC, Vilando AC, Ha TH, Lu MC (2024) Application of fluidized-bed homogeneous crystallization technology to carbon sequestration and recovery from flue gas. Sustain Environ Res 34(1):11. https://doi.org/10.1186/s42834-024-00216-y

Javaid R, Qazi UY (2019) Catalytic oxidation process for the degradation of synthetic dyes: an overview. Int J Environ Res Public Health 16(11):2066. https://doi.org/10.3390/ijerph16112066

Jiang Y, Ran J, Mao K, Yang X, Zhong L, Yang C, Feng X, Zhang H (2022) Recent progress in Fenton/Fenton-like reactions for the removal of antibiotics in aqueous environments. Ecotoxicol Environ Saf 236:113464. https://doi.org/10.1016/j.ecoenv.2022.113464

Jiang RH, Ha TH, Chiemchaisri C, Yu CW, Lu MC (2025) Application of Cu5. 5Fe1 catalyst from fluidized-bed crystallization reactor for treatment of RB5 azo dye using a Fenton-like system. J Environ Chem Eng. https://doi.org/10.1016/j.jece.2025.117483

Keselytė A, Denafas G, Ha TH, Lu MC (2025) Application of Ni-Fe catalyst from fluidized-bed crystallisation reactor for treatment of RB5 azo dye using a Fenton-like system. Process Saf Environ Prot 196:106959. https://doi.org/10.1016/j.psep.2025.106959

Khan MS, Shah JA, Riaz N, Butt TA, Khan AJ, Khalifa W, Gasmi HH, Latifee ER, Arshad M, Al-Naghi AAA, Ul-Hamid A (2021) Synthesis and characterization of Fe-TiO$_2$ nanomaterial: performance evaluation for RB5 decolorization and in vitro antibacterial studies. Nanomaterials (Basel) 11(2):436. https://doi.org/10.3390/nano11020436

Lacson CFZ, Lu MC, Huang YH (2021) Chemical precipitation at extreme fluoride concentration and potential recovery of CaF2 particles by fluidized-bed homogenous crystallization process. Chem Eng J 415:128917. https://doi.org/10.1016/j.cej.2021.128917

Lee C, Kim HH, Park NB (2018) Chemistry of persulfates for the oxidation of organic contaminants in water. Membr Water Treat 9(6):405–419. https://doi.org/10.12989/mwt.2018.9.6.405

Li WZ, Mahasti NN, Chang KY, Huang YH (2023) Application of Fe0. 66Cu0. 33@ Al (OH) 3 catalyst from fluidized-bed crystallizer by-product for RB5 azo dye treatment using visible light-assisted photo-Fenton technology. Chemosphere 343:140268. https://doi.org/10.1016/j.chemosphere.2023.140268

Liang Y, Tu Z, Wu Q, Zhang X, Tan X, Guan X, Zhao J (2025) Degradation of printing and dyeing wastewater pollutant reactive black 5 via pyrite activated persulfate: efficacy and application impact assessment. J Water Process Eng 70:107082. https://doi.org/10.1016/j.jwpe.2025.107082

Liao PL, Mahasti NNN, Huang YH (2022) The recovery of sulfur as ZnS particles from sulfide-contained wastewater using fluidized bed homogeneous crystallization technology. Chem Eng J 430:133170. https://doi.org/10.1016/j.cej.2021.133170

Liao PL, Effendi LW, Mahasti NNN, Chang KY, Huang YH (2024) Homogeneous crystallization of nickel as Ni_3S_4 in a fluidized bed reactor with supersaturation control. J Environ Chem Eng 12(6):114596. https://doi.org/10.1016/j.jece.2024.114596

Liu Y, Wang J (2023) Multivalent metal catalysts in Fenton/Fenton-like oxidation system: a critical review. Chem Eng J 466:143147. https://doi.org/10.1016/j.cej.2023.143147

Liu PC, Vilando AC, Lu MC (2022) Treatment of synthetic zinc and nickel wastewater and identification of its crystallization products by fluidized bed homogeneous crystallization technology. Process Saf Environ Prot 164:154–163. https://doi.org/10.1016/j.psep.2022.05.066

Liu HY, Vilando AC, Ha TH, Lu MC (2024) Exploring the feasibility of using fluidized bed homogeneous crystallization technology to recover sulfate ions from briny water as calcium sulfate pellets. Desalination 592:118174. https://doi.org/10.1016/j.desal.2024.118174

Lucas MS, Peres JA (2006) Decolorization of the azo dye reactive black 5 by Fenton and photo-Fenton oxidation. Dyes Pigm 71(3):236–244. https://doi.org/10.1016/j.dyepig.2005.07.007

Madlangbayan GAC, Quiton KGN, Ha TH, Lu MC (2025) Enhanced recovery of lead and nitrate via fluidized-bed reactor: recovery of insoluble salts from simulated gold cyanidation effluent. Chem Eng J. https://doi.org/10.1016/j.cej.2025.169101

Mahasti NN, Lin JY, Shih YJ, Huang YH (2022) Simultaneous recovery of Cu_2O and FeOOH from wastewater contaminated with mixed metals using fluidized-bed crystallization. J Environ Chem Eng 10(3):107357. https://doi.org/10.1016/j.jece.2022.107357

Malik S, Patel UD (2023) Catalytic activation of peroxymonosulphate with manganese and cobalt coated micro sand particles for the treatment of floor-wash containing reactive black 5 (RB5) dye. Mater Today Proc 77:1–7. https://doi.org/10.1016/j.matpr.2022.08.212

Mbarek WB, Al Harbi M, Hammami B, Khitouni M, Escoda L, Suñol JJ (2023) Nanostructured Mn–Ni powders produced by high-energy ball-milling for water decontamination from RB5 dye. Crystals 13(6):879. https://doi.org/10.3390/cryst13060879

Rambu AP, Nadejde C, Schneider RJ, Neamtu M (2018) Thin films containing oxalate-capped iron oxide nanomaterials deposited on glass substrate for fast Fenton degradation of some micropollutants. Environ Sci Pollut Res 25(7):6802–6813. https://doi.org/10.1007/s11356-017-1022-y

Rashtbari Y, Abazari M, Arfaeinia L, Gholizadeh A, Afshin S, Poureshgh Y, Alipour M (2023) The optimization of Reactive Black 5 dye removal in the sono-catalytic process combined with local yellow montmorillonite and hydrogen peroxide using response surface methodology from aqueous solutions. Biomass Convers Biorefin 13(7):6067–6081. https://doi.org/10.1007/s13399-021-01773-7

Rezaei M, Mengelizadeh N, Berizi Z, Salehnia S, Asgari M, Balarak D (2023) Synthesis of MMT− $CuFe_2O_4$ composite as a peroxymonosulfate activator for the degradation of reactive black 5. ChemistrySelect 8(2):e202201729. https://doi.org/10.1002/slct.202201729

Santos CS, Gabriel B, Blanchy M, Menes O, García D, Blanco M, Arconada N, Neto V (2015) Industrial applications of nanoparticles–a prospective overview. Mater Today Proc 2(1):456–465. https://doi.org/10.1016/j.matpr.2015.04.056

Santos PB, Dos Santos HF, Andrade GF (2021) Photodegradation mechanism of the RB5 dye: a theoretical and spectroscopic study. J Photochem Photobiol, A 416:113315. https://doi.org/10.1016/j.jphotochem.2021.113315

Sari B, Güney H, Türkeş S, Keskinkan O (2023) Reactive Black 5 removal with ozone on lab-scale and modeling. Ozone Sci Eng 45(1):50–64. https://doi.org/10.1080/01919512.2022.2035211

Sarkar P, Roy D, Bera B, De S, Neogi S (2022) Enhanced photodegradation of reactive dyes in textile effluent with $CoFe_2O_4$/g-CN heterostructure–mediated peroxymonosulphate activation. Environ Sci Pollut Res 29(33):50566–50583. https://doi.org/10.1007/s11356-022-18944-2

Shahid T, Arfan M, Zeb A, BiBi T, Khan TM (2018) Preparation and physical properties of functional barium carbonate nanostructures by a facile composite-hydroxide-mediated route. Nanomater Nanotechnol 8:1847980418761775. https://doi.org/10.1177/1847980418761775

Sharma VK, Herrmann H, Meyerstein D (2025) Carbonate radical anion (CO3•–) in carbonated water: generation and importance in environmental processes. Environ Sci Technol 59(48):25518–25526. https://doi.org/10.1021/acs.est.5c05578

Signorelli SCM, Costa JM, de Almeida Neto AF (2021) Electrocoagulation-flotation for orange II dye removal: Kinetics, costs, and process variables effects. J Environ Chem Eng 9(5):106157. https://doi.org/10.1016/j.jece.2021.106157

Tian H, Chen C, Zhu T, Zhu B, Sun Y (2021) Characterization and degradation mechanism of bimetallic iron-based/AC activated persulfate for PAHs-contaminated soil remediation. Chemosphere 267:128875. https://doi.org/10.1016/j.chemosphere.2020.128875

Tian K, Shi F, Cao M, Zheng Q, Zhang G (2022) A review of persulfate activation by magnetic catalysts to degrade organic contaminants: Mechanisms and applications. Catalysts 12(9):1058. https://doi.org/10.3390/catal12091058

Valderama VE Jr, Ballesteros FC Jr, Vilando AC, Lu MC (2025) Cu/Ni recovery by phosphate crystallization using fluidized-bed homogeneous crystallization from electroplating wastewater. Sep Purif Technol. https://doi.org/10.1016/j.seppur.2025.134287

Wang J, Wen X, Jiang S, Chen T (2022) Activation of persulfate for degrading tetracycline using the leaching residues of the lead-zinc flotation tailing. Polymers 14(14):2959. https://doi.org/10.3390/polym14142959

Wang Y, Chen F, Guo H, Sun P, Zhu T, Horn H, Liu Y (2024) Permanganate (PM) pretreatment improves medium-chain fatty acids production from sewage sludge: the role of PM oxidation and in-situ formed manganese dioxide. Water Res 249:120869. https://doi.org/10.1016/j.watres.2023.120869

Wu S, Yang Y, Deng S, Cao H, Liu Y, Yang T, Wu D, Wang C, Ma Z (2022) A novel preparation process of straw-based iron material for enhanced persulfate activation of Reactive Black 5 degradation. Environ Sci Pollut Res 29(23):34174–34185. https://doi.org/10.1007/s11356-022-18679-0

Yamanaka N, Shimazu S (2022) Selective hydrogenation properties of Ni-based bimetallic catalysts. Eng 3(1):60–77. https://doi.org/10.3390/eng3010006

Yu Z, Sun Q, Zhang L, Yang H, Chen Y, Guo J, Zhang M, Zhang Z, Jiang Y (2024) Research progress of amorphous catalysts in the field of electrocatalysis. Microstructures 4(2):100871. https://doi.org/10.1016/j.checat.2023.100871

Zhou Y, Lu J, Zhou Y, Liu Y (2019) Recent advances for dyes removal using novel adsorbents: a review. Environ Pollut 252:352–365. https://doi.org/10.1016/j.envpol.2019.05.072

Zhu S, Li X, Kang J, Duan X, Wang S (2018) Persulfate activation on crystallographic manganese oxides: Mechanism of singlet oxygen evolution for nonradical selective degradation of aqueous contaminants. Environ Sci Technol 53(1):307–315. https://doi.org/10.1021/acs.est.8b04669

Zhu Y, Cao Y, Shu S, Zhu P, Wang D, Xu H, Cai D (2023a) Comparison of medium-pressure UV/peracetic acid to remove three typical refractory contaminants of textile wastewater. Processes 11(4):1183. https://doi.org/10.3390/pr11041183

Zhu Y, Xie Q, Deng F, Ni Z, Lin Q, Cheng L, Chen X, Qiu R, Zhu R (2023b) The differences in heterogeneous Fenton catalytic performance and mechanism of various iron minerals and their influencing factors: a review. Sep Purif Technol 325:124702. https://doi.org/10.1016/j.seppur.2023.124702